Magnitude and phase calibration of lock-in amplifiers, and analysis of the noise response

Magnitude and Phase Calibration of Lock-In Amplifiers, and Analysis of the Noise Response

Alessandro Cultrera, Juan Medved, *Graduate Student Member, IEEE*, Paolo Durandetto, Massimo Ortolano, Andrea Sosso, and Luca Callegaro, *Member, IEEE*

***Abstract*— In this work, a method for the calibration of the magnitude and phase of lock-in amplifiers (LIAs) and the characterization of their noise response are presented. A simple calibration setup developed at INRIM is used to calibrate the magnitude and phase of digital LIAs. These quantities are typically loosely or not specified, respectively, by the manufacturers. Furthermore, since the low-pass filter of a LIA can introduce correlations, which may affect the correct estimation of the measurement type A uncertainty, the noise response of this instrument has been analyzed in terms of the Allan deviation for an autoregressive (AR) low-pass filter with different orders. The presented approach was tested on three units of the same instrument, proving to be consistent but also showing some unit-to-unit differences. The present results show that for the considered measurement settings a substantial improvement of the accuracy of LIAs up to the 10 kHz range can be obtained with commercial instrumentation. The magnitude error can be determined with about a 50-fold improvement in accuracy compared to the specifications of the tested instruments; the phase error, which is not specified, can be determined at the same time. The proposed method also requires a short time per calibration point (a few minutes).**

***Index Terms*— Calibration, digital filters, metrology, noise, signal reconstruction.**

I. Introduction

LOCK-IN amplifiers (LIAs) are the most popular signal recovery instruments [1], [2], [3], [4], [5]. They are employed in countless physics and engineering laboratory experiments involving small electrical signals. A number of measurement setups use LIAs as small voltage (or current) vector meters, the instrument reading is related to the value of the physical quantity of interest [6], [7], [8], [9], [10], [11].

Among the several examples that not only require sensitivity but also good accuracy in LIA measurements there are classical and quantum Hall effect experiments. For instance, in the recent surge of quantum anomalous Hall effect experiments (e.g., [12, Fig. 3.3], [13], [14, Fig. S2], [15]), one or more LIAs are employed to determine the quantization conditions with driving currents in the nanoampere range.

The specified base accuracy of a commercial LIA is typically around 1%, which can have a significant impact on the measurement uncertainty of the quantity of interest. A proper route to improve the overall measurement accuracy includes: 1) the calibration of the LIA's magnitude and phase and 2) the characterization of the LIA's noise response, since its low-pass filter can introduce correlations that can affect the zero detection threshold and the proper evaluation of the type A measurement uncertainty component. It is also worth mentioning that the lock-in technique is the basis of some impedance analyzer implementations employed in applications involving weak signals [16], [17].

In recent years, National Metrology Institutes have been developing techniques [18], [19], [20], [21] for the traceable calibration of the magnitude error of LIAs in the voltage reading mode. A summary of the methods employed and of the corresponding performances of these implementations is reported in Table I.

In 2020, INRIM and METAS (the Swiss national metrology institute) performed an intercomparison [20], [23] to mutually validate their calibration capabilities. A popular LIA model (Stanford Research SR850), available since the 1990s, was employed as the transfer standard.

In this work, we describe the progress made on the characterization of LIAs. The experimental activity focuses on a more recent instrument model, a Zurich Instruments (ZI) mid-frequency lock-in (MFLI) amplifier 500 kHz, with the determination of its magnitude and phase errors in the presence of a phase shift between the calibration signal and the reference signal, and the characterization of the instrument noise response as a function of its low-pass filter order. However, this characterization strategy can be applied to other LIA models (provided some information about the implemented signal processing chain is available, e.g., SR850 manual [24] page 3-12).

This work is a technically extended version of [25]. The article is structured in two parts. In the first part, the calibration

Received 4 November 2024; revised 17 February 2025; accepted 27 February 2025. Date of publication 24 March 2025; date of current version 29 April 2025. This work has been supported by the project CAPSTAN Quantum electrical Italian national capacitance standard funded by the MIUR Progetti di Ricerca di Rilevante Interesse Nazionale (PRIN) Bando 2020, grant 2020A2M33J. This work was supported by the European Union under the Horizon Europe in the Framework of the EMPHASIS project (https://www.emphasissupercaps.eu/) under Grant 101091997. However, the views and opinions expressed are those of the authors only, and do not necessarily reflect those of the European Union or the Horizon Europe Program. Neither the European Union nor the granting authority can be held responsible for them. The identification of commercial equipment in this work does not imply recommendation or endorsement by the authors, nor that the equipment identified is necessarily the best available for the purpose. The Associate Editor coordinating the review process was Dr. Benkuan Wang. *(Corresponding author: Alessandro Cultrera.)*

Alessandro Cultrera, Paolo Durandetto, Andrea Sosso, and Luca Callegaro are with the Istituto Nazionale di Ricerca Metrologica (INRIM), 10135 Turin, Italy (e-mail: a.cultrera@inrim.it).

Juan Medved is with INRIM and Politecnico di Torino (POLITO), 10129 Turin, Italy.

Massimo Ortolano is with Politecnico di Torino (POLITO), 10129 Turin, Italy.

Digital Object Identifier 10.1109/TIM.2025.3553954

TABLE I
LITERATURE SURVEY ABOUT LIA CALIBRATION METHODS

Reference	Method	Frequency range	Amplitude	Phase	Best reported uncertainty
Theocarous [22]	Photodiode excited by tunable light flux; linearity only, no absolute calibration.	40 Hz – 70 Hz	2 mV – 200 mV	No	Unspecified
Raso [18]	2-output digital source, AC voltmeter, 1250:1 resistive divider.	20 Hz – 1 kHz	Unspecified	Yes	Unspecified
Corminboeuf [19]	3-output digital source, sampling voltmeter, inductive divider, step-down transformer chain.	20 Hz – 10 kHz	100 nV – 100 µV	No	70 µV/V, (10 µV, 100 Hz)
Georgakopoulos [21]	Josephson array waveform synthesizer.	60 Hz – 1 kHz	1 µV – 1 mV	No	100 µV/V, (10 mV, 1 kHz)
Cultrera [20]	3-output digital source, sampling voltmeter, inductive and resistive dividers.	20 Hz – 1 kHz	100 nV – 10 µV	No	100 µV/V, (10 µV, 100 Hz)
This work	3-output digital source, sampling voltmeter, inductive and resistive dividers, multiplexer.	100 Hz – 10 kHz	1 µV – 10 µV	Yes	200 µV/V and 0.08 mrad, (10 µV, 3 kHz, 45°)

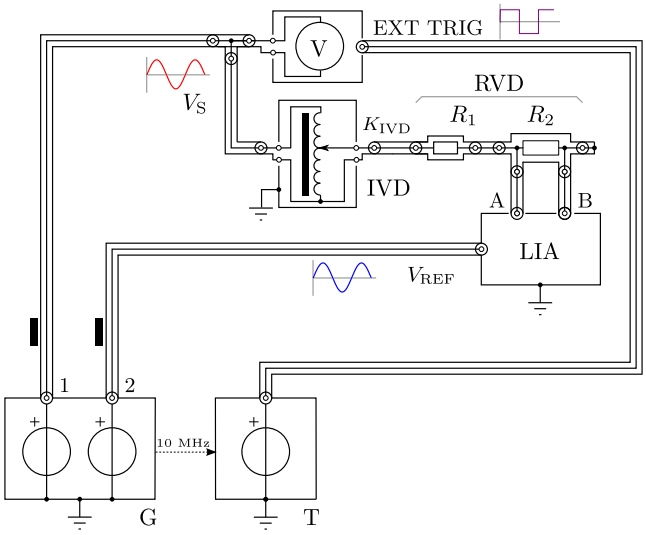

Fig. 1. Schematic of the calibration setup. The legend of the labels employed is given in the text of Section II and in Table II.

of the magnitude and phase of LIAs is discussed; in the second part, the noise response of LIAs is addressed. The experimental setup for calibration is presented in Section II; the related quantities of interest and measurement model are introduced in Section III; the results of calibration are discussed in Section IV. In the part on noise response, the theoretical analysis of filter response is treated in Section V-A and experimental results are discussed in Section V-B. The article includes also three Appendices (A–C) that provide more details on the determination and uncertainty estimation of the quantities related to the calibration signal.

II. EXPERIMENTAL SETUP AND SIGNAL PATHS

The calibration setup is presented schematically in Fig. 1 and the list of the equipment employed is given in Table II.

The setup includes two function generators: G (Keysight 33520B), with two output channels, and T (Keysight 32250A), with one output channel. G generates two low-distortion and stable sinusoidal signals with nominal root mean square (rms) values of 1 V: channel 1 drives the calibration signal chain and channel 2 provides a reference signal. G also delivers a 10 MHz time base to T. The signal from channel 1 of G is measured by the calibrated sampling voltmeter V (Agilent 3458A), triggered at the EXT TRIG input by the transistor–transistor-logic-compatible (TTL) signal generated by T, and then scaled down to the level of interest by the inductive voltage divider IVD (Electro Scientific Industries PRT-73) cascaded with the resistive voltage divider RVD (composed of the four-terminal pair standard resistors HP 42035A and HP 42039A). The output of RVD at the high voltage (A) and low voltage (B) terminals of R_2 yields the calibration signal driving the differential input of the LIA under calibration (ZI MFLI 500 kHz). This is also provided by the reference signal from channel 2 of G. The setup includes also two current equalizers, represented in Fig. 1 by two black rectangles.

A personal computer (not shown in Fig. 1) controls G, T, V, and IVD through an IEEE 488 interface. The LIAs are controlled through a USB interface and the operating parameters are set through the proprietary web-browser interface ZI LabOne. This interface allows an operator to save and recall the instrument settings using XML format files; these settings may include hardware configuration (e.g., aux input/output ports assignment), measurement settings (e.g., filter order n, Sync filter mode), and the interface appearance. The controlling application is written in MATLAB employing the Instrument Control toolbox and the ZI application program interface.

In the following, the three ZI MFLI tested units are labeled LIA-1 (serial no. 7144 with options MF-MD and MF-IA), LIA-2 (serial no. 6236 with option MF-DIG), and LIA-3 (serial no. 3596 with options MF-MD and MF-IA).

III. MEASUREMENT MODELS

This section presents the quantities of interest for the calibration and the measurement model. The fundamental

TABLE II
INSTRUMENTATION AND EQUIPMENT EMPLOYED IN THE SETUP REPRESENTED IN FIG. 1

Symbol	instrument	model
G	2-channel waveform generator	Keysight 33520B
T	1-channel waveform generator	Keysight 32250A
V	Digital voltmeter	Agilent 3458A, DCV digitising function, TRIG EXT mode
IVD	Inductive voltage divider	Electro Scientific Instruments PRT-73, 7-decade automatic precision ratio transformer, 0.35 V/Hz option
RVD	Resistive voltage divider	Composed of R_1 and R_2
R_1	100 kΩ	HP 42039A defined as a two-terminal resistor
R_2	10 Ω	HP 42035A defined as a four-terminal resistor
	Current equalisers	Purpose-built devices

components at frequency f_{CAL} of the voltage signals in the system are represented by complex phasors. The phasors V_S (source voltage) and V_{REF} (reference voltage) represent the fundamental components of channels 1 and 2 of G, respectively. The superscripts "nom" and "read" label nominal quantity values and LIA readings, respectively.

The phasor V_{CAL} representing the calibration voltage can be written as

$$V_{CAL} = k_{CAL} V_S = k_{RVD} k_{IVD} V_S \tag{1}$$

where k_{CAL} is the overall ratio of the cascaded voltage dividers, k_{RVD} is the ratio of the RVD, and k_{IVD} is the ratio of the IVD. The above frequency-dependent complex quantities can be expressed in polar form as

$$\begin{aligned} V_{CAL} &= |V_{CAL}| e^{j\varphi_{CAL}} \\ k_{RVD} &= |k_{RVD}| e^{j\varphi_{RVD}} \\ k_{IVD} &= |k_{IVD}| e^{j\varphi_{IVD}} \\ V_S &= |V_S| e^{j\varphi_S} \end{aligned} \tag{2}$$

where φ_{CAL} represents the phase of V_{CAL} with respect to V_{REF}; φ_{IVD} and φ_{RVD} represent the phase deviations introduced by IVD and RVD, respectively; and φ_S represents the phase of V_S with respect to V_{REF} with nominal value $\varphi_S^{nom} = \varphi_{CAL}^{nom}$. The forms (2) allow us to expand (1) as

$$|V_{CAL}| e^{j\varphi_{CAL}} = |k_{RVD}||k_{IVD}||V_S| e^{j\varphi_{RVD}} e^{j\varphi_{IVD}} e^{j\varphi_S} \tag{3}$$

with $|V_{CAL}| = |k_{RVD}||k_{IVD}||V_S|$ and $\varphi_{CAL} = \varphi_{RVD} + \varphi_{IVD} + \varphi_S$.

The magnitude and phase errors of the LIA driven by the signals V_{CAL} and V_{REF} are defined in Sections III-A and III-B below.

A. LIA Magnitude Error

The relative magnitude error δR introduced by the LIA in the measurement of V_{CAL} can be defined as

$$\delta R = \frac{|V_{CAL}^{read}|}{|V_{CAL}|} - 1 \tag{4}$$

where V_{CAL}^{read} is obtained from the LIA readings V_{LIA}^{read} subtracting the offset V_{OS}^{read} obtained with $k_{IVD} = 0$ such that

$$|V_{CAL}^{read}| e^{j\varphi_{CAL}^{read}} = |V_{LIA}^{read}| e^{j\varphi_{LIA}^{read}} - |V_{OS}^{read}| e^{j\varphi_{OS}^{read}}. \tag{5}$$

The definition (4) can be expanded using (3) as

$$\delta R = \frac{|V_{CAL}^{read}|}{|k_{RVD}||k_{IVD}||V_S|} - 1 \tag{6}$$

which coincides with the definition already given in [20].

TABLE III
LIA SETTINGS

Parameter	Setting
Signal input	Differential
Reference	External, at frequency f_{CAL} (see text)
Coupling	DC
Range	1 mV
Time constant	100 ms
Low pass filter order (n)	1, 8
Synchronous filter (Sync)	Off, On (if $f < 200$ Hz and $n = 1$)
Output sampling frequency (f_{SO})	13.08 Hz

B. LIA Phase Error

The phase error $\Delta\varphi$ introduced by the LIA in the measurement of V_{CAL} can be defined as

$$\Delta\varphi = \varphi_{CAL}^{read} - \varphi_{CAL} \tag{7}$$

which, taking into account (3), can be written as

$$\Delta\varphi = \varphi_{CAL}^{read} - (\varphi_{RVD} + \varphi_{IVD} + \varphi_S) \tag{8}$$

where the offset has been already compensated from (5).

IV. CALIBRATION OF MAGNITUDE AND PHASE

LIAs are complex instruments for which the measurement outcome strongly depends on a number of measurement settings. For this reason, the calibration of δR and $\Delta\varphi$ shall be performed in a well-defined measurement configuration and considered valid only for that configuration. Considering the present LIA settings, the per-point calibration duration is of about 3 min.

A. LIA Settings and Operation

Each calibration is performed fixing the settings of G (V_S, V_{REF}, f_{CAL}, φ_S^{nom}), and T (f_s), LIA, and of the IVD to obtain the desired V_{CAL}^{nom}. For this work, $|V_{CAL}^{nom}|$ was set in the range (1–10) μV and $\varphi_{CAL}^{nom} = 45°$. Tables III and IV report the relevant LIA settings and the chosen frequency calibration points, respectively.

B. Calibration Steps

The calibration procedure consists of the following steps.

1) *Initialization:* G is set to generate V_S on channel 1 and V_{REF} on channel 2, both at frequency f_{CAL} and phase φ_S^{nom}. T is set to generate a frequency f_S chosen to be

TABLE IV
FREQUENCY CALIBRATION POINTS

f/Hz	f_s/Hz
97	97000
293	99913
997	99700
2971	95072
4987	99740
9973	99730

an integer multiple of f_{CAL}. The LIA is configured by loading the XML file.

2) *Determination of φ_S:* This is performed by connecting to the calibration setup described in Section II, a multiplexer and a digitizer which acquire both channels of G. The typical duration of this step is 120 s. This procedure is required periodically, depending on the stability of the instrumentation. This step is described in detail in Appendix A.
3) *Determination of V_{OS}^{read}:* The IVD is set to $k_{IVD}^{nom} = 0$; V_{OS}^{read} is measured by acquiring the LIA output buffer at frequency f_{SO} for 60 s.
4) *Determination of V_S:* V is used to coherently sample V_S from a minimum of $N = 20$ periods to a maximum of 20 s, depending on f_{CAL}. This step is described in detail in Appendix B.
5) *Determination of V_{LIA}^{read}:* k_{IVD}^{nom} is set to m; V_{LIA}^{read} is measured by acquiring the LIA output buffer for 60 s.
6) Steps 3 to 5 are repeated for $m = 0.01, \ldots, 0.1$ to cover the calibration signal amplitude range of interest.
7) *Estimation of δR and $\Delta\varphi$:* The magnitude and phase errors along with their uncertainty are estimated using V_{LIA}^{read}, V_{OS}^{read} and V_{CAL} as input quantities for the measurement models (6) and (8).

C. Results and Discussion

In the following, we report: 1) the calibration of LIA-1 with a detailed uncertainty budget at $f = 2971$ Hz for $|V_{CAL}| = 5$ μV, $\varphi_{CAL}^{nom} = 45°$ and low-pass filter order $n = 8$; and 2) the comparison of the calibrations of LIA-1, LIA-2, and LIA-3.

1) LIA-1 Calibration: Fig. 2(a) shows the magnitude error δR, defined as in (6), as a function of $|V_{CAL}|$ and for low-pass filter orders $n = 1$ and 8.

The magnitude error ranges from -2 mV/V to -1 mV/V. No substantial dependence on n is observed, suggesting that the mean deviation is due to the LIA gain error whereas variations across individual values are due to LIA nonlinearity. Consistent results were obtained in several other repetitions of the same calibration, with occasional discrepancy between results obtained at lower amplitude with different n's due to noise [see for example the phase error corresponding to $|V_{CAL}| = 2$ μV in Fig. 3(b)]. The uncertainty bars represent the combined standard uncertainty (coverage factor $k = 1$), which is of the order of 0.5 mV/V for $n = 1$ and less for $n = 8$. These results are within the LIA specification for the *voltage gain inaccuracy* of 1 % = 10 mV/V, up to 50 kHz. Hence, the present calibration improves the voltage gain accuracy by about one order of magnitude or better compared to the specifications.

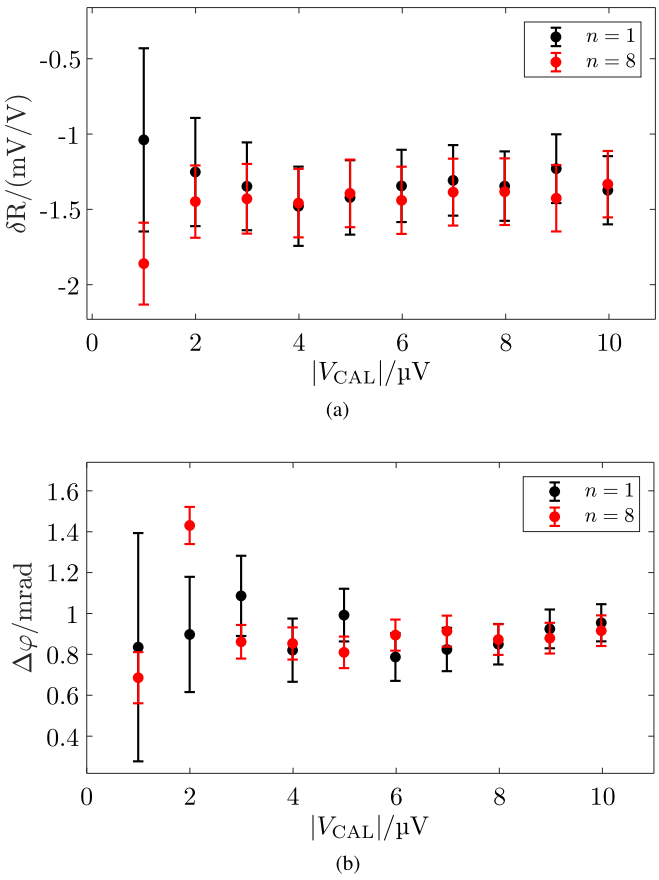

Fig. 2. Magnitude and phase calibration of LIA-1 for $|V_{CAL}^{nom}|$ from 1 to 10 μV, with the settings of Table III and $f_{CAL} = 2971$ Hz and $\varphi_{CAL}^{nom} = 45°$. Comparison of filter order settings $n = 1$ (black) and $n = 8$ (red). Uncertainty bars represent combined standard uncertainty. (a) Magnitude error δR as a function of $|V_{CAL}|$. (b) Phase error $\Delta\varphi$ as a function of $|V_{CAL}|$.

The uncertainty budget of δR for $|V_{CAL}^{nom}| = 5$ μV is reported in Table V. The uncertainty contribution of the magnitude of V_{CAL}^{read} are obtained from the readings' standards deviation of the mean of the real part of V_{LIA}^{read} subtracted of V_{OS}^{read}. The uncertainty of the magnitude of V_S is treated in depth in Appendix B, while the uncertainty components of the magnitude of the factors k_{RVD} and k_{IVD} are treated in Appendix C (a corresponding evaluation process occurred for the phase uncertainty components). The individual sensitivity coefficients are determined from the model (6) and the propagation of the uncertainty is performed according to the Guide to the expression of uncertainty in measurement (GUM) [26]. The main contribution is represented by the voltage divider RVD, which is dominated by the accuracy of the ac resistance.

Fig. 2(b) reports the phase error $\Delta\varphi$, defined as in (8), as a function of $|V_{CAL}|$ and for low-pass filter orders $n = 1$ and 8. Most values are in the range from 0.7 mrad to 1.1 mrad with no apparent dependence on n as in the previous case. $\Delta\varphi$ can be likely attributed to the phase mismatch between the LIA input and reference channels. The variation across the values is likely due to the nonlinearity introduced by the demodulation process. The uncertainty bars represent the combined standard

TABLE V
UNCERTAINTY BUDGET FOR δR FOR $|V_{\mathrm{CAL}}^{\mathrm{NOM}}| = 5\,\mu\mathrm{V}$, $\varphi_{\mathrm{CAL}}^{\mathrm{NOM}} = 45°$, $f_{\mathrm{CAL}} = 2971\,\mathrm{Hz}$, AND $n = 8$ FOR LIA-1

Quantity	x_i	$u(x_i)$	Type/Dist.	c_i	$u_i(\delta R)$
$\lvert V_{\mathrm{CAL}}^{\mathrm{read}}\rvert$	$4.981\,53 \times 10^{-6}\,\mathrm{V}$	$0.000\,11 \times 10^{-6}\,\mathrm{V}$	A/Norm.	$2.00 \times 10^{5}\ \mathrm{V}^{-1}$	$0.022\,\mathrm{mV/V}$
$\lvert V_{\mathrm{S}}\rvert$	$0.997\,337\ \mathrm{V}$	$0.000\,043\ \mathrm{V}$	B/Rect.	$1.00\ \mathrm{V}^{-1}$	$0.043\,\mathrm{mV/V}$
$\lvert k_{\mathrm{RVD}}\rvert$	$1.000\,36 \times 10^{-4}$	$0.000\,21 \times 10^{-4}$	B/Rect.	9.98×10^{3}	$0.209\,\mathrm{mV/V}$
$\lvert k_{\mathrm{IVD}}\rvert$	$5.000\,000 \times 10^{-2}$	$0.000\,032 \times 10^{-2}$	B/Rect.	2.00×10^{1}	$0.006\,\mathrm{mV/V}$
δR	$-1.394\ \mathrm{mV/V}$		RSS		$0.215\,\mathrm{mV/V}$

TABLE VI
UNCERTAINTY BUDGET FOR $\Delta\varphi$ FOR $|V_{\mathrm{CAL}}^{\mathrm{NOM}}| = 5\ \mu\mathrm{V}$, $\varphi_{\mathrm{CAL}}^{\mathrm{NOM}} = 45°$, $f_{\mathrm{CAL}} = 2971\,\mathrm{Hz}$, AND $n = 8$ FOR LIA-1

Quantity	x_i/rad	$u(x_i)/\mathrm{rad}$	Type/Dist.	c_i	$u_i(\Delta\varphi)/\mathrm{mrad}$
$\varphi_{\mathrm{CAL}}^{\mathrm{read}}$	0.783 623	0.000 021	A/Norm.	1	0.021
φ_{S}	0.782 352	0.000 073	A/Norm.	1	0.073
φ_{RVD}	0.000 461 257	0.000 000 033	B/Rect.	1	<0.001
φ_{IVD}	0.000 000 0	0.000 001 7	B/Rect.	1	<0.001
$\Delta\varphi$	0.000 809		RSS		0.077

uncertainty and for $n = 8$ are of the order of 0.15 mrad, and for phase measurements a correction of the order of 0.9 mrad is possible in the present measurements conditions.

The uncertainty budget of $\Delta\varphi$ is reported in Table VI. The individual sensitivity coefficients are determined from the model (8) and the propagation of the uncertainty is performed according to the GUM. In this case, the main contribution is represented by the uncertainty component of φ_{S}.

For the phase measurement, the instrument specifications [27] do not provide any information about the accuracy. Likewise, other LIA manufacturers do not typically provide any information on the phase accuracy. The phase resolution is sometimes specified.

The results obtained for other calibration points are consistent with those presented above. For $f < 200\,\mathrm{Hz}$ and $n = 1$ the Sync filter was used, which did not introduce any substantial additional correlation in the LIA readings at the considered f_{SO}. Calibrations were also performed at $\varphi_{\mathrm{CAL}}^{\mathrm{nom}} = 0°, 90°$, without substantial differences in the results; this is reasonable owing to the digital nature of the demodulation process.

2) Comparison of Three LIAs: The calibration as described in Section IV-C1 was applied to three units of the same instrument model.

Fig. 3 reports δR and $\Delta\varphi$ for LIA-1, LIA-2, and LIA-3, for $|V_{\mathrm{CAL}}| = 5\ \mu\mathrm{V}$, $\varphi_{\mathrm{CAL}}^{\mathrm{nom}} = 45°$, and $n = 8$ as a function of f_{CAL}. The results show a similar behavior of the LIAs, and point out that with the present setup and calibration, it is possible to reveal the distinct behavior of each unit.

Within the uncertainty, the error δR, reported in Fig. 3(a) is constant in frequency within the considered interval for all the units. Nevertheless, a slightly different frequency dependence can be observed for LIA-2 compared to the other units.

On the other hand, as shown in Fig. 3(b), the behavior of $\Delta\varphi$ can be considered linear in frequency with very similar frequency dependence for the three units. This is likely due to the different transfer functions of the low-pass filters of the LIA input and reference channels (this difference is loosely specified in [27]). In fact, at low frequency, a low pass filter typically introduces a linear phase shift, and a mismatch of the transfer functions of the input and reference channels generates a linear phase error.

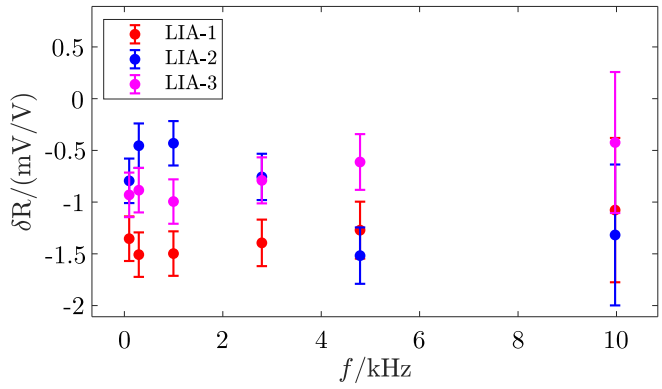

(a)

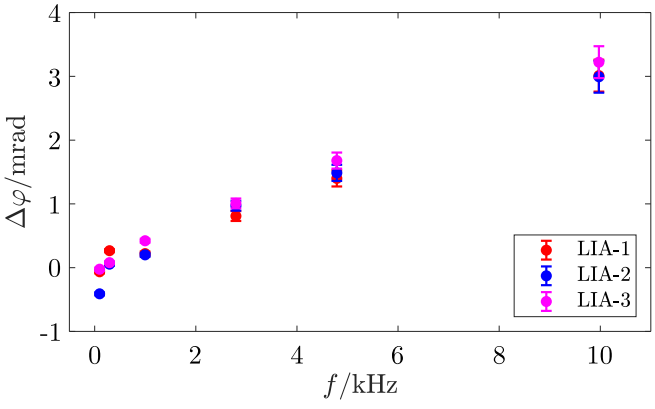

(b)

Fig. 3. Comparison of the magnitude and phase calibration of LIA-1 (red), LIA-2 (blue) and LIA-3 (magenta) with $|V_{\mathrm{CAL}}^{\mathrm{nom}}| = 5\ \mu\mathrm{V}$, $\varphi_{\mathrm{CAL}}^{\mathrm{nom}} = 45°$, and $n = 8$, as a function of f_{CAL}; LIAs set as per Table III. Uncertainty bars represent combined standard uncertainty. (a) Magnitude error δR as a function of f_{CAL}. (b) Phase error $\Delta\varphi$ as a function of f_{CAL}.

In both cases, uncertainty bars increase at higher f_{CAL}. This is due to the IVD contribution to the uncertainty (see Appendix C).

The errors δR and $\Delta\varphi$ as a function of f_{CAL} for other values of $|V_{\mathrm{CAL}}|$ within the considered range (not reported here) are consistent with the presented ones. Note that the considered LIA units can be considered reasonably representative of other commercially available instruments of the same nominal characteristics and the proposed calibration can be in principle applied to any digital LIA of interest.

It is worth briefly discussing the possible effects of temperature on the present calibration. This calibration chain is implemented with commercial equipment with specifications given for a reasonably wide temperature range 23(5) °C, while the HP42030 resistors used in the experiment have a 10 μΩ/Ω°C temperature coefficient. The ZI MFLI manual gives an input amplitude stability of the gain of 0.1 %/°C and a stability of 0.05 μHz/Hz°C at 23 °C for the internal frequency reference. The calibrations took place in a temperature-controlled laboratory 23.0(5) °C. The effects of temperature fluctuations in the lab during the calibration process (≈0.3 °C over 30 min), provided having any effect on the instrument temperature, can be considered negligible for the present accuracy level. However, to maintain the accuracy of such a calibration, an instrument should be calibrated at the same location and temperature where it will be used.

The calibration results (with the setup of II) are traceable to the international system of units (SI). Traceability is achieved by calibration of each component of the calibration setup of Fig. 1, performed by INRIM in its capacity of Italian National Metrology Institute. V is calibrated with traceability to the Italian national standard of electric voltage; IVD is calibrated with the setup of the primary ac voltage ratio standard; R_1 and R_2 are calibrated by direct comparison with the maintained resistors of the national standard of ac resistance. The calibration uncertainties are in line with the INRIM calibration and measurement capabilities (CMCs), as declared in the framework of the International Committee for Weights and Measures Mutual Recognition Arrangement (CIPM MRA) on the Key Comparison DataBase (KCDB) [28].

V. Noise Response

When performing voltage or current measurements with an LIA, operating either as zero detector or as vector meter, the correlations introduced by the LIA low-pass filter and the aliasing effect introduced by the output filter downsampler can affect either the zero detection threshold or the type A uncertainty component of the meter measurements, generally leading to the underestimation of the type A uncertainty or the assumption of too low a detection threshold. These parameters can be suitably represented by an estimate of the standard deviation of the mean of a sequence of repeated measurements or by an estimate of their Allan deviation, with the latter being applicable to a broader family of noise processes [29], [30], [31]. It is thus worth investigating how an LIA responds to a noisy input by determining how the aforementioned parameters depend on the LIA filter time constant, its order, and sampling rate. Reference [32] reports a detailed analysis, both theoretical and experimental, of the standard deviation of the mean and of the Allan deviation of voltage measurements performed by an LIA with a moving-average filter up to the fourth order when the input is driven by a white noise source. The ZI MFLI considered in this work operates instead with an autoregressive (AR) filter up to the eighth order [27], and its noise response is analyzed in this section. We limit our analysis to the Allan deviation because, in addition to the broader applicability mentioned above, it has unbiased estimators whose uncertainty can be calculated in a reasonably straightforward way [33], thus allowing for a better comparison between theory and experiment.

A. Theoretical Analysis of the LIA Filter Noise Response

Like most modern LIAs, the ZI MFLI is a digital instrument. The input signal is first band-limited by an anti-aliasing filter and then digitized with fixed sampling frequency $f_{\mathrm{SI}} = 60\,\mathrm{MHz}$ [27] and sampling period $T_{\mathrm{SI}} = 1/f_{\mathrm{SI}}$. The synchronous demodulation is performed digitally. The output of the demodulator filter is downsampled by an integer factor D to yield the output sampling frequency $f_{\mathrm{SO}} = f_{\mathrm{SI}}/D$, settable by the user from about 0.102 Hz to 857 kHz. This is also the rate at which the LIA output data are transmitted to a data server and recorded on a computer. In the following, we shall assume negligible aliasing at the input, but we shall account for the aliasing caused by the output downsampling. The type of processing outlined above is implemented in digital LIAs of other brands as well (e.g., [24], [34]) and the validity of the ensuing analysis is by no means limited to the ZI MFLI.

In our experimental setup, as in [32], the LIA voltage input is driven by the thermal noise generated by a resistor R kept at the thermodynamic temperature T. Indeed, the following analysis is not tied to this specific noise source, but it is valid for any input signal (voltage or current) corrupted by white noise (or approximately white in a narrow bandwidth around the reference frequency).

We perform the analysis in the frequency domain, considering two-sided spectral density functions defined for Fourier frequencies f such that $-\infty < f < +\infty$. We represent the input noise voltage generated by the resistor by a random process $N(t)$ with associated two-sided spectral density function $S_N(f) \approx h_0/2$, with $h_0 = 4k_B T R$ and k_B being the Boltzmann's constant. The bandwidth of the input noise voltage is limited to a cut-off frequency f_{H} by the interconnection to the LIA and by the anti-aliasing filter. The digitized samples can be represented by the random sequence $N_k = N(kT_{\mathrm{SI}})$, k integer. Assuming negligible aliasing at this stage, the spectral density function of the sequence N_k is $S_N(f)$ for $|f| \lessapprox f_{\mathrm{H}} < f_{\mathrm{SI}}/2$, where $f_{\mathrm{SI}}/2$ is the input Nyquist frequency.

The real samples N_k are multiplied by the complex reference sequence $r_k = \sqrt{2}\mathrm{e}^{\mathrm{j}2\pi f_{\mathrm{R}} k T_{\mathrm{SI}}}$, with f_{R} being the reference frequency (here we consider $f_{\mathrm{R}} \ll f_{\mathrm{H}}$), and then filtered by the LIA low-pass filter, which is an AR(n) filter with n coincident poles [27] and transfer function

$$H(f) = \left(\frac{1 - \mathrm{e}^{-T_{\mathrm{SI}}/T_{\mathrm{N}}}}{1 - \mathrm{e}^{-T_{\mathrm{SI}}/T_{\mathrm{N}}}\mathrm{e}^{-2\mathrm{j}\pi f T_{\mathrm{SI}}}}\right)^n \tag{9}$$

$$\approx \left(\frac{1}{1+\mathrm{j}2\pi f T_\mathrm{N}}\right)^n \tag{10}$$

where T_N is the LIA time constant. The approximation (10), which shows that the AR(n) filter emulates an analog n-order filter, holds for $f \ll f_\mathrm{SI}$ and $T_\mathrm{N} \gg T_\mathrm{SI}$, and these inequalities are fulfilled in virtually all operating conditions of practical interest. The above chain of operations—multiplication by a reference signal and filtering—generates a complex random sequence Z'_k with spectral density function [35]

$$S_{Z'}(f) = 2S_N(f - f_\mathrm{R})|H(f)|^2 \approx h_0|H(f)|^2. \tag{11}$$

The sequence Z'_k is downsampled at the output sampling frequency $f_\mathrm{SO} = f_\mathrm{SI}/D$ to generate the sequence $Z_k = Z'_{\mathrm{D}k}$. The LIA low-pass filter may operate as an anti-aliasing filter, but its effectiveness depends on the operator's choice of parameters. Therefore, the aliasing cannot be considered negligible at this stage, and the spectral density function of Z_k is [35]

$$S_Z(f) = \sum_{l=-\infty}^{+\infty} S_{Z'}(f - l f_\mathrm{SO}) \approx h_0 \sum_{l=-\infty}^{+\infty} |H(f - l f_\mathrm{SO})|^2. \tag{12}$$

The real and imaginary parts of Z_k, $X_k = \mathrm{Re}\, Z_k$ and $Y_k = \mathrm{Im}\, Z_k$, constitute the X and Y output channels of the LIA. Without loss of generality, let us now consider the X channel. The sequence X_k has spectral density function

$$S_X(f) = \frac{1}{4}\big[S_Z(f) + S_Z(-f)\big] = \frac{S_Z(f)}{2} \tag{13}$$

where the last equality holds for the evenness of $S_Z(f)$.

We now determine the Allan variance at the averaging times $\tau_j = m_j T_\mathrm{SO}$, $m_j = 2^{j-1}$, $j = 1, 2, \ldots$ We choose the τ_j's to be powers-of-two multiples of T_SO for compatibility with the Allan variance estimator used in Section V-B below. Let

$$G_{m_j}(\nu) = \frac{\sin^4(\pi \nu m_j)}{m_j^2 \sin^2(\pi \nu)} \tag{14}$$

then the Allan variance of the sequence X_k at the averaging time τ_j is given by [36]

$$\sigma^2_{\bar{X}}(\tau_j) = 2\int_{-f_\mathrm{SO}/2}^{f_\mathrm{SO}/2} G_{m_j}(f T_\mathrm{SO}) S_X(f)\,\mathrm{d}f \tag{15}$$

$$= 4 f_\mathrm{SO} \int_0^{1/2} G_{m_j}(\nu) S_X(\nu f_\mathrm{SO})\,\mathrm{d}\nu \tag{16}$$

$$= 2 f_\mathrm{SO} h_0 \int_0^{1/2} G_{m_j}(\nu) \sum_{l=-\infty}^{+\infty} |H[(\nu - l) f_\mathrm{SO}]|^2\,\mathrm{d}\nu \tag{17}$$

where in (16), we have exploited the evenness of $S_X(f)$ and normalized the frequency with respect to f_SO, $\nu = f/f_\mathrm{SO}$. The limits of integration in (15) are $\pm f_\mathrm{SO}/2$, where $f_\mathrm{SO}/2$ is the output Nyquist frequency. The normalized output Nyquist frequency in (16) and (17) is thus 1/2. The integral in (17) can be solved numerically provided that the infinite summation is suitably truncated to a finite one. To this purpose, since the upper limit of the integral is 1/2, let us include in the summation all l's such that $|H[(1/2 - l) f_\mathrm{SO}]|^2 > \epsilon$, where ϵ is a small number. From this condition we get a maximum index $l_\mathrm{max}(\epsilon) = \lceil 0.5 + 2\pi f_\mathrm{SO} T_\mathrm{N} \epsilon^{1/2n} \rceil$, where $\lceil x \rceil$ denotes the smallest integer greater than or equal to x. Therefore, (17) can be rewritten as

$$\sigma^2_{\bar{X}}(\tau_j, \epsilon) = 2 f_\mathrm{SO} h_0 \int_0^{1/2} G_{m_j}(\nu) \sum_{l=-l_\mathrm{max}(\epsilon)}^{+l_\mathrm{max}(\epsilon)} |H[(\nu - l) f_\mathrm{SO}]|^2\,\mathrm{d}\nu. \tag{18}$$

We can then analyze the convergence of (18) with respect to ϵ, or that of the Allan deviation $\sigma_{\bar{X}}(\tau_j, \epsilon)$. For example, consider the data of Fig. 5(g) with $T_\mathrm{N} \approx 0.1$ s, $n = 1$, $f_\mathrm{SO} \approx 102.2$ mHz and $j = 1$ ($\tau_1 = T_\mathrm{SO}$), which is the case with the highest aliasing. Table VII reports $\sigma_{\bar{X}}(\tau_1, \epsilon)$ for four values of ϵ, chosen in a decreasing geometric progression, and the corresponding values of $L_\mathrm{max}(\epsilon)$. The last two columns of Table VII report the differences $\Delta\sigma_{\bar{X}}(\tau_1, \epsilon_k) = \sigma_{\bar{X}}(\tau_1, \epsilon_k) - \sigma_{\bar{X}}(\tau_1, \epsilon_{k-1})$ and the ratios $\Delta\sigma_{\bar{X}}(\tau_1, \epsilon_{k-1})/\Delta\sigma_{\bar{X}}(\tau_1, \epsilon_k)$. It can be observed that the difference of each iteration with respect to the previous one decreases by a constant factor. This suggests that the convergence of (18) for a choice of the ϵ's in geometric progression follows a geometric progression as well. This type of convergence allows the application of the Aitken's Δ^2-process for the acceleration of convergence to extrapolate a better estimate of $\sigma_{\bar{X}}(\tau_j)$ as [37, §3.9(iii)]

$$\tilde{\sigma}_{\bar{X}}(\tau_j) = \frac{\sigma_{\bar{X}}(\tau_j, \epsilon_k)\sigma_{\bar{X}}(\tau_j, \epsilon_{k+2}) - \sigma^2_{\bar{X}}(\tau_j, \epsilon_k)}{\sigma_{\bar{X}}(\tau_j, \epsilon_k) - 2\sigma_{\bar{X}}(\tau_j, \epsilon_{k+1}) + \sigma_{\bar{X}}(\tau_j, \epsilon_{k+2})}. \tag{19}$$

For instance, the extrapolated Allan deviation $\tilde{\sigma}_{\bar{X}}(\tau_1)$ from the data of Table VII is 63.54 nV. With this process, from the analysis of all measurement data, it is safe to expect a worst case error in the computation of $\sigma_{\bar{X}}(\tau_j)$ well below 1 % for the parameters used in this work, thus virtually negligible with respect to the experimental uncertainty.

Disregarding aliasing and LIA filtering, (17) yields

$$\sigma^2_{\bar{X},0}(\tau_j) = 2 f_\mathrm{SO} h_0 \int_0^{1/2} G_{m_j}(\nu)\,\mathrm{d}\nu = \frac{h_0}{2\tau_j} \tag{20}$$

which is the well-known result of the Allan variance of white noise. This result will be used in Section V-B as a reference to emphasize the effects of filtering, correlation, and aliasing.

B. Results and Discussion

Fig. 4 reports the schematic of the circuit employed to measure the LIA noise response. The LIA A input is driven by the white noise generated by the 100 kΩ resistor R (a Vishay Z foil resistor with a low-temperature coefficient and low excess noise) at an ambient temperature of about 22 °C. The temperature is not controlled but monitored through a precision negative temperature coefficient (NTC) thermistor, which is attached to the body of R. The digital multimeter DMM measuring the NTC thermistor resistance is connected before the start of a noise response measurement, disconnected during the measurement, and reconnected after the end of the measurement. The temperature is stable within 0.5 °C for the duration of any measurement. Taking into account the 10 MΩ LIA input resistance in parallel to the 100 kΩ

TABLE VII
CONVERGENCE OF (18) WITH RESPECT TO ϵ

k	ϵ_k	$L_{\max}(\epsilon_k)$	$\sigma_{\bar{X}}(\tau_1,\epsilon_k)/\mathrm{nV}$	$\Delta\sigma_{\bar{X}}(\tau_1,\epsilon_k)/\mathrm{nV}$	$\frac{\Delta\sigma_{\bar{X}}(\tau_1,\epsilon_{k-1})}{\Delta\sigma_{\bar{X}}(\tau_1,\epsilon_k)}$
1	10^{-2}	157	61.51		
2	10^{-3}	494	62.90	1.39	
3	10^{-4}	1559	63.33	0.43	3.09
4	10^{-5}	4927	63.47	0.14	3.07

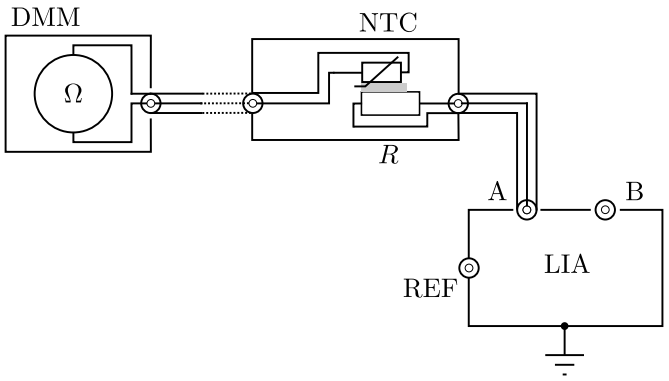

Fig. 4. Schematic of the circuit employed to measure the LIA noise response: R is a 100 kΩ Vishay Z foil resistor; NTC is a precision thermistor attached to the body of R; DMM is a digital multimeter measuring the NTC thermistor resistance at the beginning and at the end of a measurement.

resistance, the equivalent resistance is about 99 kΩ, yielding $h_0 \approx 1.6 \times 10^{-15}\,\mathrm{V^2/Hz}$. The bandwidth of the input noise voltage is mainly limited by the first-order low-pass filter composed of R, the cable capacitance, and the LIA input capacitance, with −3 dB cut-off frequency $f_{\mathrm{H}} \approx 19\,\mathrm{kHz}$. The effect of the LIA input noise, whose spectral density function is about $6.3 \times 10^{-18}\,\mathrm{V^2/Hz}$ above 1 kHz [27], is practically negligible.

Fig. 5 reports the computed and measured Allan deviations of the LIA X channel for a selection of measurements performed in this work. All reported measurements were performed with $f_{\mathrm{R}} = 1\,\mathrm{kHz} \ll f_{\mathrm{H}}$ and $T_{\mathrm{N}} \approx 0.1\,\mathrm{s}$; for the plots on the left, $n = 1$; for those on the right, $n = 8$; from top to bottom f_{SO} decreases and the effect of aliasing becomes increasingly significant. The solid lines represent the theoretical Allan deviations $\tilde{\sigma}_{\bar{X}}(\tau_j)$ computed according to theory presented in Section V-A. The dashed lines represent the Allan deviation $\sigma_{\bar{X},0}(\tau_j) = \sqrt{h_0/(2\tau_j)}$ predicted by (20) for an unfiltered white noise of the same level and in absence of aliasing. The circles with uncertainty bars represent the values $\hat{\sigma}_{\bar{X}}(\tau_j)$ estimated from the measurements. These values and their uncertainties were determined from the estimated values of the *Haar wavelet variance*, according to the connection between this and the Allan variance established in [31][1]

$$\sigma^2_{\bar{X}}(\tau_j) = 2\nu^2_{\bar{X}}(\tau_j) \tag{21}$$

[1]These computations were performed with the help of the MATLAB wavelet toolbox which implements all the needed algorithms. See in particular the functions `modwt` and `modwtvar`.

where $\nu^2_{\bar{X}}(\tau_j)$ is the Haar wavelet variance at scale τ_j. In this case, $\tau_j = m_j T_{\mathrm{SO}}$ with $m_j = 2^{j-1} \leqslant N/2$, where N is the number of samples recorded in a measurement.

The measured values are compatible with the theoretical values. The behavior of the Allan deviation exhibited in Fig. 5(a)–(d) is typical of an LIA when aliasing is negligible. For $\tau_j \ll T_{\mathrm{N}}$, $\sigma_{\bar{X}}(\tau_j) < \sigma_{\bar{X},0}(\tau_j)$ because the LIA filter reduces the noise bandwidth; besides, $\sigma_{\bar{X}}(\tau_j)$ increases with τ_j because the LIA filter correlates the readings as well. For $\tau_j \gg T_{\mathrm{N}}$, the readings become uncorrelated and $\sigma_{\bar{X}}(\tau_j) \approx \sigma_{\bar{X},0}(\tau_j)$.

The behavior of the Allan deviation in Fig. 5(a)–(d) can also be intuitively understood by looking at Fig. 6, showing the transfer functions that appear in the integrand of (17) for an example case in which aliasing is almost negligible ($n = 1$, $T_{\mathrm{N}} = 0.02\,\mathrm{s}$ and $f_{\mathrm{SO}} \approx 104.6\,\mathrm{Hz}$). The transfer function $|H(\nu f_{\mathrm{SO}})|$ (solid red line in Fig. 6) of the LIA low-pass filter has a cut-off frequency which is much less than the Nyquist frequency; therefore, its aliases $|H[(\nu - l) f_{\mathrm{SO}}]|$, $l \neq 0$, (dashed red lines) have almost negligible magnitude in the frequency range $0 \leqslant \nu < 1/2$ with respect to $|H(\nu f_{\mathrm{SO}})|$, and $\sum_{l=-\infty}^{\infty} |H[(\nu - l) f_{\mathrm{SO}}]| \approx |H(\nu f_{\mathrm{SO}})|$ (solid black line). Then, it can be seen that the function $G_1(\nu)$ (blue solid line) corresponds to a high-pass filter, whereas a function $G_{m_j}(\nu)$ corresponds to a bandpass filter approximately over the frequency range from $1/(4m_j)$ to $1/(2m_j)$ (see also [36] on this). Therefore, for small m_j's (i.e., short integration times τ_j's), $G_{m_j}(\nu)$ selects a frequency range in which the input white noise is already attenuated by $|H(\nu f_{\mathrm{SO}})|$, and the Allan deviation is much less than the one corresponding to the unfiltered white noise, as shown in Fig. 5(a)–(d) for $\tau_j \lessapprox 1\,\mathrm{s}$. For large m_j's (i.e., long integration times τ_j's), the transfer function $G_{m_j}(\nu)$ moves toward the left of Fig. 6 and selects a frequency range in which $H(\nu f_{\mathrm{SO}}) \approx 1$. In this case, the Allan deviation is approximately that of the unfiltered white noise, as shown in Fig. 5(a)–(d) for $\tau_j \gg 1\,\mathrm{s}$.

Fig. 5(e)–(g) shows the effect of aliasing. The measured and computed Allan deviations are greater than the one predictable for white noise without aliasing represented by the dashed lines: $\sigma_{\bar{X}}(\tau_j)/\sigma_{\bar{X},0}(\tau_j) \approx 3.5$ for Fig. 5(e); $\sigma_{\bar{X}}(\tau_j)/\sigma_{\bar{X},0}(\tau_j) \approx 1.6$ for Fig. 5(f); $\sigma_{\bar{X}}(\tau_j)/\sigma_{\bar{X},0}(\tau_j) \approx 7.0$ for Fig. 5(g); $\sigma_{\bar{X}}(\tau_j)/\sigma_{\bar{X},0}(\tau_j) \approx 3.2$ for Fig. 5(h). The lower the sampling frequency, the higher the aliased variance because more aliases contribute to the effective noise. In addition, it can be observed that the effect of aliasing is greater for $n = 1$ with respect to $n = 8$. The reason is that as discussed above the LIA low-pass filter behaves like an anti-aliasing filter, and the higher the order of the filter, the better is the anti-aliasing action.

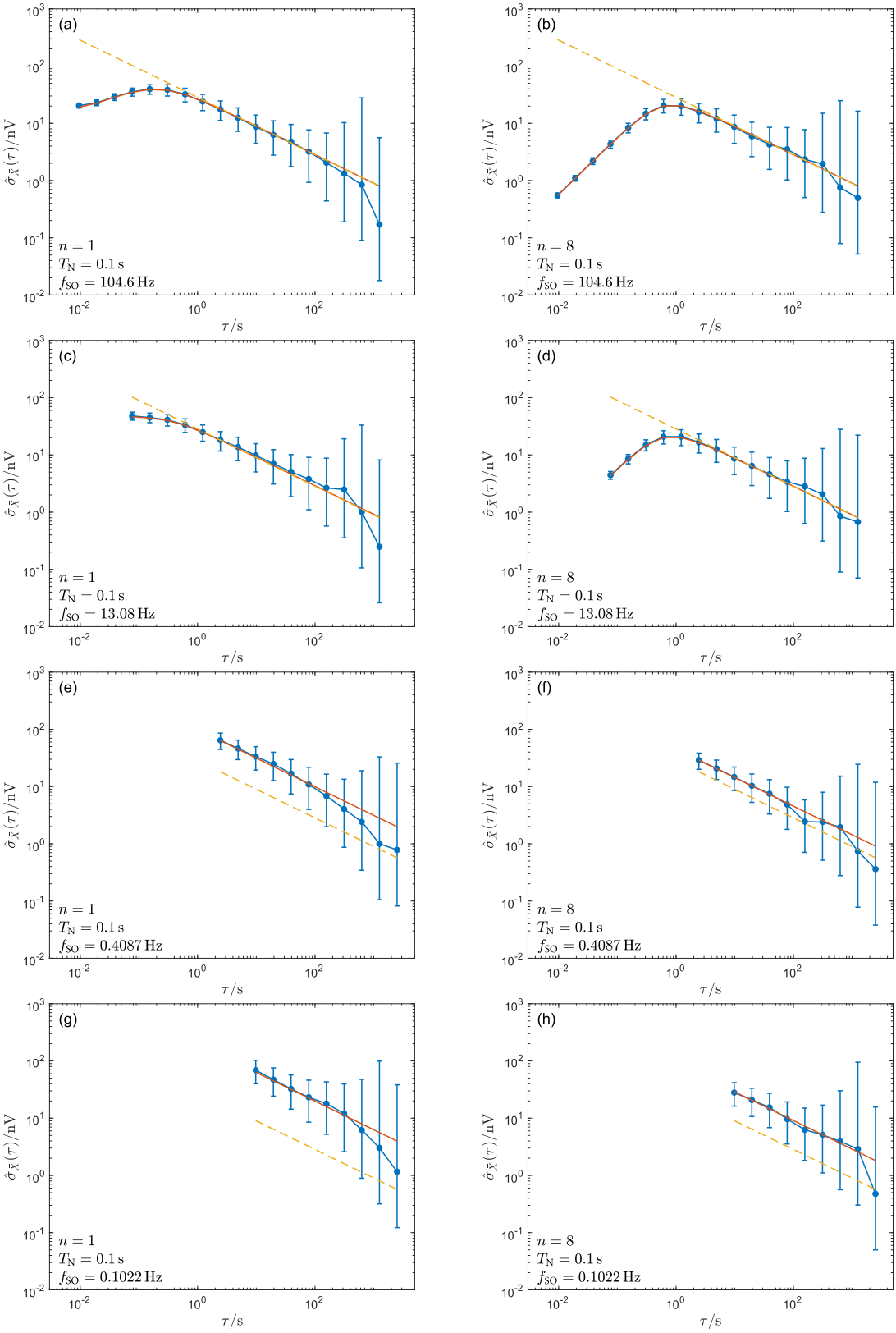

Fig. 5. Computed $\tilde{\sigma}_{\bar{X}}(\tau)$ (solid lines) and estimated $\hat{\sigma}_{\bar{X}}(\tau)$ Allan deviations (circles with uncertainty bars) of the LIA X channel for the filters of order 1 (left) and 8 (right) with variable sampling frequency when the input is driven by the white noise generated by a resistor. The dashed lines represent the Allan deviation $\sigma_{\bar{X},0}(\tau)$ expected for an unfiltered white noise of the same level and in the absence of aliasing. The reference frequency is $f_R = 1\,kHz$ and $\tau = \tau_j = 2^{j-1}T_{SO}$, $j = 1, \ldots, N/2$, N is the number of samples taken for each measurement (variable from figure to figure). The plots (a), (c), (e), and (g) report the results for the filter order $n = 1$, with decreasing output sampling frequency from top to bottom; similarly, the plots (b), (d), (f), and (h) report the results for the filter order $n = 8$.

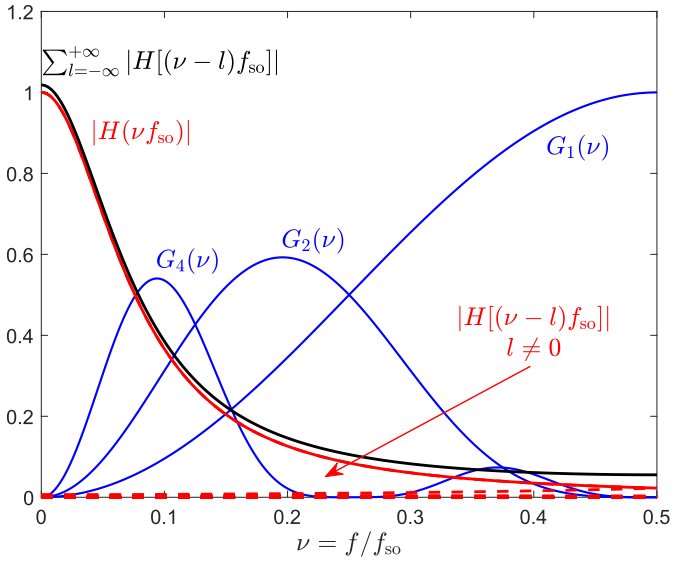

Fig. 6. Transfer functions appearing in the integrand of (17) for $n = 1$, $T_N = 0.02\,s$, and $f_{SO} \approx 104.6\,Hz$, parameters for which aliasing is almost negligible.

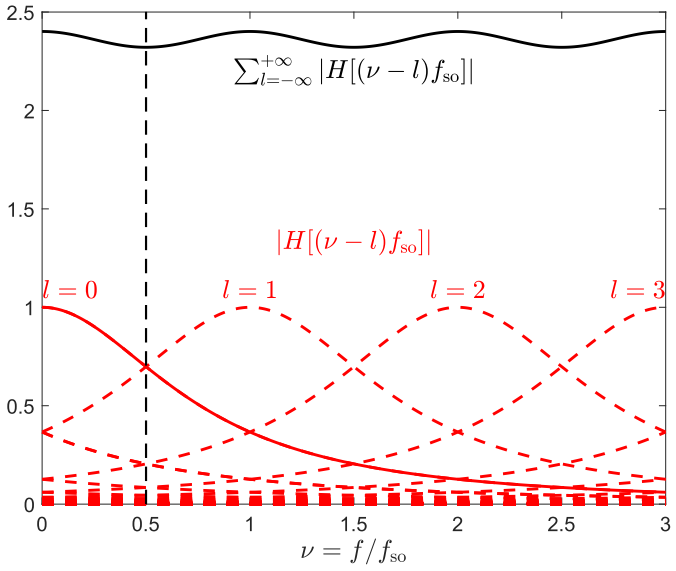

Fig. 7. Transfer functions appearing in the integrand of (17) for $n = 1$, $T_N = 0.02\,s$, and $f_{SO} \approx 10.46\,Hz$, parameters for which aliasing is no longer negligible.

The behavior of the Allan deviation in Fig. 5(e)–(g) can also be intuitively understood by looking at Fig. 7, showing the transfer functions that appear in the integrand of (17) for an example case in which aliasing is no longer negligible ($n = 1$, $T_N = 0.02\,s$, and $f_{SO} \approx 10.46\,Hz$). The transfer functions are plotted with an extended frequency axis to better represent the aliases $|H[(\nu-l)f_{SO}]|$ for a few values of l (red lines in Fig. 7; solid line for $l = 0$; dashed lines for $l \neq 0$). The aliases overlap significantly and (solid black line) $\sum_{l=-\infty}^{\infty}|H[(\nu-l)f_{SO}]| > 1$ and almost constant in the frequency range $0 \leqslant \nu < 1/2$, implying that the input white noise is amplified and almost unfiltered. As a consequence, the Allan deviation follows the white noise behavior, but at a level higher than that of the input noise, as can be seen in Fig. 5(e)–(g). This "whitening" effect is typical of aliasing.

TABLE VIII
DGS TRIGGER SUBSYSTEM PARAMETERS

Layer	Source	Count	Delay	Ecount
Arm:layer 2	IMM	1	auto	1
Arm:layer 1	EXT	40	auto	200 000
Trigger	EXT	100 000	auto	1

VI. CONCLUSION

The present setup and calibration allow for a substantial improvement of the measurement accuracy of both magnitude and phase (over an extended frequency range) of LIAs. This can be of interest in several experiments involving LIAs in the audio frequency range, especially considering that the instrument's specifications are often not thorough in this aspect. Unit-to-unit differences can be revealed, indicating the potential worthiness of the calibration of a specific unit. We also remark that a clear knowledge of the instrument filtering effects is fundamental for a proper choice of measurement settings and a correct interpretation of the results. In addition, unlike other proposed methods that require several custom parts, this method involves only commercial instrumentation and components.

APPENDIX A
DETERMINATION OF THE SOURCE VOLTAGE PHASE

The estimation of the phase error $\Delta\varphi$ as defined in (8) requires an accurate estimation of φ_{CAL}, which depends on φ_S. The measurement of φ_S is performed by connecting the setup shown in Fig. 8 to the calibration setup of Fig. 1.

The idea is to alternately digitize with the same instrument, in a coherent way for an integer number of periods, the two channels of G, periodically exchanging the two channels to compensate for the asymmetries in the measuring paths.

The digitizer DGS is a Fluke 8588A reference multimeter connected to G through the purpose-built multiplexer MUX. The generator G is initialized to generate V_S on channel 1 and V_{REF} on channel 2 at frequency f. The generator T is initialized to drive the DGS external trigger input EXT TRIG IN at frequency f_S with TTL-compatible levels. The DGS trigger subsystem is set as in Table VIII.

The measurement sequence is as follows. First, the operator connects channels 1 and 2 of G to channels 1 and 2 of MUX, respectively. This is called the *forward* (F) configuration. DGS records *Trigger Count* samples of channel 1 of G, then drives MUX to switch to channel 2, skips *Arm: layer 1 Ecount* samples, and records *Trigger Count* samples of channel 2. This sequence is repeated in reverse order, first digitizing channel 2 again and then channel 1, such that the channels are sampled *Arm: layer 1 Count* times in the sequence 1221. The operator now connects channels 1 and 2 of G to channels 2 and 1 of MUX, respectively, running again the above-described digitizing sequence. This is called the *reverse* (R) configuration. The discrete Fourier transforms of the samples in the two configurations are employed to obtain the forward phase $\varphi_S^F = \arg(V_S/V_{REF})$ and the reverse phase $\varphi_S^R = \arg(V_{REF}/V_S)$ from the fundamental components of the two signals.

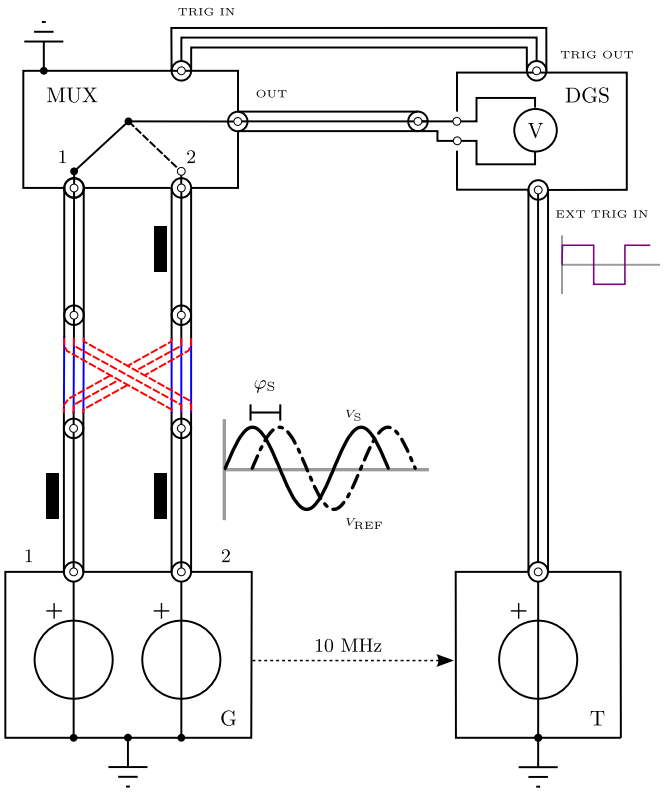

Fig. 8. Schematic of the measurement of φ_S. Solid lines between G and MUX represent the forward measurement configuration. Dashed lines represent the reverse configuration.

From φ_S^F and φ_S^R, the source phase φ_S can be obtained as

$$\varphi_S = \frac{\varphi_S^F - \varphi_S^R}{2} \tag{22}$$

thus canceling with the differential measurement possible systematic errors.

As an example, considering $f_{CAL} = 9973$ Hz and $\varphi_{CAL}^{nom} = 45°$, we determined $\varphi_S = 44.30°$. The phase measurements pointed out that φ_S has a drift of the order of 10μrad over a week, likely due to the fluctuating loading conditions of the generator channels. This means that step 2 of Section IV-B may be skipped if repeated calibrations are performed in a short time span.

APPENDIX B
DETERMINATION OF THE SOURCE VOLTAGE MAGNITUDE

The estimation of the magnitude error δR as defined in (6) requires an accurate estimation of the magnitude $|V_{CAL}|$, which depends on $|V_S|$. A comprehensive analysis of the accuracy of V (Agilent 3458A used in DCV digitizing mode) has been taken into account, considering the extensive knowledge on the topic provided by literature [38], [39], [40].

The source signal V_S is coherently sampled with V on its 10 V range, triggered by T at the frequencies f_S reported in Table IV.

To optimize the tradeoff between communication speed and digitizing resolution of V, the data format is set to single-INT (SINT) and the aperture time t_A is set to 1.4 μs. This yields a resolution of 16 bit, corresponding to about 366 μV on the 10 V range.

The raw data acquired using the DCV digitizing function of V are processed with a discrete Fourier transform algorithm, extracting the fundamental component $|V_{DMM}|$. This is corrected as discussed in the following to determine $|V_S|$.

A. Estimation and Uncertainty Evaluation

The mathematical model that provides the corrected magnitude of V_S is

$$|V_S| = k_{DC}|k_{AC}||V_{DMM}| \tag{23}$$

where the correction factor k_{DC} is the dc gain of V and k_{AC} is the frequency response of V, a complex quantity of which we consider the magnitude in this case. Each of these can be expanded as

$$k_{DC} = k_{DCG}k_{GA} \tag{24}$$

and

$$k_{AC} = k_{SINC}k_{ACG}k_{DF} \tag{25}$$

where the individual factors in (24) and (25) are discussed in the following.

1) DC Corrections (k_{DC}): The k_{DCG} factor in (24) represents the part of the dc gain of V which can be attributed to the internal voltage reference as well as to the instrument's input stage. We assumed $k_{DCG} = 1$ with a relative uncertainty of approximately 15 μV/V obtained from the 2-year dc accuracy specifications of V for a voltage of 1 V in the 10 V range.

The factor k_{GA} represents the part of the dc gain due to the ADC at short aperture times, which is specific to the particular unit [38], [39]. This factor has been experimentally determined in the 10 V range by measuring three stable dc voltages sampled: 1) a short-circuit; 2) the 1.018 V; and 3) 10 V, where the last two voltages were generated by a Fluke 732B voltage standard. These voltages were measured both with the dc voltage function (NPLC = 50) and with the DCV digitizing function at $f_S = 100$ kHz and $t_A = 1.4$ μs. A fitting of the digitized values versus the values measured with the dc voltage function yielded $k_{GA} = 9(20)$ μV/V with an offset of about 2.3 mV. Although this offset is not negligible, it does not impact the ac voltage measurements presented in this work.

2) AC Corrections (k_{AC}): The overall frequency-dependent response of V is influenced by three distinct factors. The first term in (25) arises from the behavior of the ADC, which integrates the input signal over the aperture time t_A. The ADC integration implies a low-pass filtering that depends on both t_A and f, an effect commonly referred to as the "sinc" filter. The corresponding gain correction factor k_{SINC} is given by

$$k_{SINC} = \frac{\pi f t_A}{\sin(\pi f t_A)} = \text{sinc}^{-1}(\pi f t_A). \tag{26}$$

The uncertainty associated with this correction is negligible, since it depends on the individual f and t_A uncertainties: the signal frequency f uncertainty is 1 μHz/Hz from the specifications of G, whereas the uncertainty of t_A is assumed to be 50 ps [41].

TABLE IX
EXAMPLE OF UNCERTAINTY BUDGET OF $|V_S|$ AT $f_{CAL} = 97$ Hz (IN THE FOLLOWING TABLES A ZERO INDICATES NEGLIGIBLE CONTRIBUTION)

Quantity	x_i	$u(x_i)$	c_i	$u_i(\|V_S\|)$
Type A				
$\|V_{DMM}\|$	0.997 290 V	14×10^{-6} V	1.000 011	14 µV
Type B				
k_{DCG}	1.000 000	15×10^{-6}	0.997 301 V	15 µV
k_{GA}	1.000 009	20×10^{-6}	0.997 292 V	20 µV
$\|k_{SINC}\|$	1.000 000	0	0.997 301 V	0 µV
$\|k_{ACG}\|$	1.000 000	0	0.997 301 V	0 µV
$\|k_{DF}\|$	1.000 002	1×10^{-6}	0.997 299 V	1 µV
Combined				
$\|V_S\|$	0.997 301 V			29 µV

The other frequency-dependent corrections arise from bandwidth effects. The front-end circuitry of V for the 10 V range is assumed to behave as a single-pole low-pass filter described by

$$k_{ACG}^{-1} = \frac{V_{OUT}}{V_{IN}} = \frac{1}{\sqrt{1 + (f/f_C)^2}} \tag{27}$$

with nominal -3 dB corner frequency $f_C = 120$ kHz [40]. Moreover, a slight frequency roll-off could also be linked to input capacitance dissipation, whose transfer function can be modeled as

$$k_{DF}^{-1} = 1 - f\, t_{DF} \tag{28}$$

t_{DF} being the dissipation factor time constant. In [38] and [41], the input frequency responses of two different 3458A digital voltmeter units were accurately measured and modeled with the $k_{ACG}^{-1}k_{DF}^{-1}$ transfer function. Optimal parameters were shown to be in the range $f_C = 117(2)$ kHz and $t_{DF} = 25(10)$ ns for both units. Assuming that these values are applicable to our unit, along with the previously discussed "sinc" correction, the total ac gain correction $|k_{AC}|$ deviates from unity gain by 2 µV/V at 100 Hz and increases up to 0.4 % at 10 kHz.

Considering all the correction factors and measurement repeatability, uncertainty budget examples for $|V_S|$ at the considered f_{CAL} values are presented in Tables IX–XIV. At low frequency ($f < 1$ kHz), the main source of uncertainty is due to dc gain corrections. As f increases, ac effects become more prominent, with the larger contribution stemming from input filter and input capacitance dissipation losses. Nevertheless, the overall uncertainty across all signal frequencies remains significantly lower than the uncertainty of the voltage divider. The combined standard uncertainty, presented in the bottom-right corner of each table, is assessed following the guidelines provided in the GUM. All the input quantities are assumed to follow a normal distribution.

APPENDIX C
FREQUENCY RESPONSE OF THE VOLTAGE DIVIDER

As described in Section II, the voltage divider is composed of an IVD cascaded with an RVD. The frequency response of the voltage divider and its contribution to the calibration uncertainty is described here. A schematic representation of the voltage divider is shown in Fig. 9.

TABLE X
EXAMPLE OF UNCERTAINTY BUDGET OF $|V_S|$ AT $f_{CAL} = 293$ Hz

Quantity	x_i	$u(x_i)$	c_i	$u_i(\|V_S\|)$
Type A				
$\|V_{DMM}\|$	0.997 468 V	14×10^{-6} V	1.000 019	14 µV
Type B				
k_{DCG}	1.000 000	15×10^{-6}	0.997 487 V	15 µV
k_{GA}	1.000 009	20×10^{-6}	0.997 478 V	20 µV
$\|k_{SINC}\|$	1.000 000	0	0.997 487 V	0 µV
$\|k_{ACG}\|$	1.000 003	0	0.997 484 V	0 µV
$\|k_{DF}\|$	1.000 007	3×10^{-6}	0.997 480 V	3 µV
Combined				
$\|V_S\|$	0.997 487 V			29 µV

TABLE XI
EXAMPLE OF UNCERTAINTY BUDGET OF $|V_S|$ AT $f_{CAL} = 997$ Hz

Quantity	x_i	$u(x_i)$	c_i	$u_i(\|V_S\|)$
Type A				
$\|V_{DMM}\|$	0.997 334 V	11×10^{-6} V	1.000 073	11 µV
Type B				
k_{DCG}	1.000 000	15×10^{-6}	0.997 407 V	15 µV
k_{GA}	1.000 009	20×10^{-6}	0.997 398 V	20 µV
$\|k_{SINC}\|$	1.000 003	0	0.997 404 V	0 µV
$\|k_{ACG}\|$	1.000 036	1×10^{-6}	0.997 371 V	1 µV
$\|k_{DF}\|$	1.000 025	10×10^{-6}	0.997 382 V	10 µV
Combined				
$\|V_S\|$	0.997 407 V			29 µV

TABLE XII
EXAMPLE OF UNCERTAINTY BUDGET OF $|V_S|$ AT $f_{CAL} = 2971$ Hz

Quantity	x_i	$u(x_i)$	c_i	$u_i(\|V_S\|)$
Type A				
$\|V_{DMM}\|$	0.996 837 V	12×10^{-6} V	1.000 433	12 µV
Type B				
k_{DCG}	1.000 000	15×10^{-6}	0.997 269 V	15 µV
k_{GA}	1.000 009	20×10^{-6}	0.997 260 V	20 µV
$\|k_{SINC}\|$	1.000 028	0	0.997 241 V	0 µV
$\|k_{ACG}\|$	1.000 322	11×10^{-6}	0.996 948 V	11 µV
$\|k_{DF}\|$	1.000 074	30×10^{-6}	0.997 195 V	30 µV
Combined				
$\|V_S\|$	0.997 269 V			42 µV

TABLE XIII
EXAMPLE OF UNCERTAINTY BUDGET OF $|V_S|$ AT $f_{CAL} = 4987$ Hz

Quantity	x_i	$u(x_i)$	c_i	$u_i(\|V_S\|)$
Type A				
$\|V_{DMM}\|$	0.996 115 V	15×10^{-6} V	1.001 122	15 µV
Type B				
k_{DCG}	1.000 000	15×10^{-6}	0.997 233 V	15 µV
k_{GA}	1.000 009	20×10^{-6}	0.997 224 V	20 µV
$\|k_{SINC}\|$	1.000 080	0	0.997 153 V	0 µV
$\|k_{ACG}\|$	1.000 908	31×10^{-6}	0.996 328 V	31 µV
$\|k_{DF}\|$	1.000 125	50×10^{-6}	0.997 108 V	50 µV
Combined				
$\|V_S\|$	0.997 233 V			66 µV

The overall ratio of the voltage divider is $k_{CAL} = k_{RVD}k_{IVD}$, where k_{IVD} is the ratio of the *unloaded* IVD and k_{RVD} is

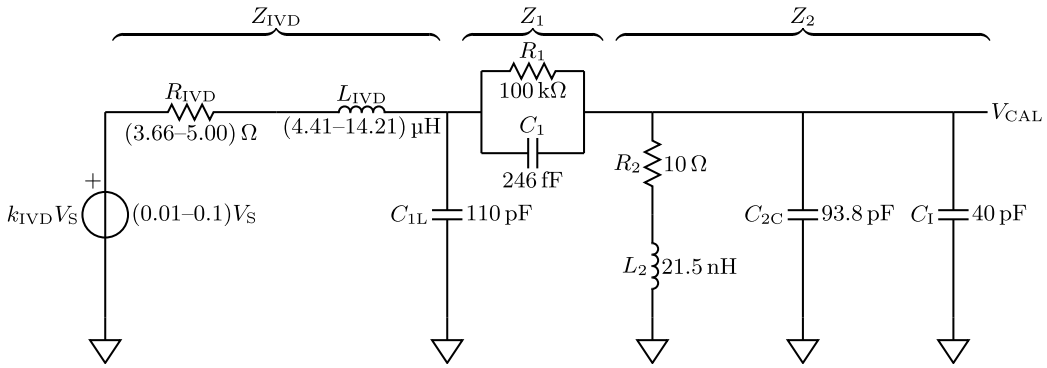

Fig. 9. Schematic representation of the cascaded voltage dividers IVD and RVD, loaded by the LIA. Relevant reported parameters are discussed in the text.

TABLE XIV
EXAMPLE OF UNCERTAINTY BUDGET OF $|V_{\mathrm{S}}|$ AT $f_{\mathrm{CAL}} = 9973$ Hz

Quantity	x_i	$u(x_i)$	c_i	$u_i(\lvert V_{\mathrm{S}}\rvert)$
Type A				
$\lvert V_{\mathrm{DMM}}\rvert$	0.993 307 V	30×10^{-6} V	1.004 207	30 µV
Type B				
k_{DCG}	1.000 000	15×10^{-6}	0.997 486 V	15 µV
k_{GA}	1.000 009	20×10^{-6}	0.997 477 V	20 µV
$\lvert k_{\mathrm{SINC}}\rvert$	1.000 321	0	0.997 166 V	0 µV
$\lvert k_{\mathrm{ACG}}\rvert$	1.003 626	124×10^{-6}	0.993 882 V	123 µV
$\lvert k_{\mathrm{DF}}\rvert$	1.000 249	100×10^{-6}	0.997 238 V	100 µV
Combined				
$\lvert V_{\mathrm{S}}\rvert$	0.997 486 V			163 µV

the ratio of the RVD including the loading of the IVD. IVD is modeled by an ideal voltage source $k_{\mathrm{IVD}}V_{\mathrm{S}}$ with equivalent output impedance $Z_{\mathrm{IVD}} = R_{\mathrm{IVD}} + \mathrm{j}2\pi f L_{\mathrm{IVD}}$, where R_{IVD} and L_{IVD} were measured experimentally. C_{1L} (measured) is the interconnection capacitance from IVD to R_1 of RVD. This resistor is modeled by the impedance $Z_1 = R_1/(1+\mathrm{j}2\pi f R_1 C_1)$ composed of the resistance R_1 with stray capacitance C_1 (from the calibration certificate). The resistor R_2 is modeled by the resistance R_2 in series with the stray inductance L_2 (from the calibration certificate). C_{2C} is the interconnection capacitance from R_2 to the LIA input and C_I is the LIA input capacitance (from specifications [27]). All these elements form the impedance Z_2. The LIA input resistance has been neglected because it affects the ratio at about the 1×10^{-6} level. From the equivalent circuit of Fig. 9, the RVD ratio is given by

$$k_{\mathrm{RVD}} = \frac{1}{(1 + Z_1/Z_2)(1 + Z_{\mathrm{IVD}}/Z_{\mathrm{RVD}})} \tag{29}$$

from which

$$k_{\mathrm{CAL}} = \frac{1}{(1 + Z_1/Z_2)(1 + Z_{\mathrm{IVD}}/Z_{\mathrm{RVD}})} k_{\mathrm{IVD}}. \tag{30}$$

The uncertainty contribution of the voltage divider ratio k_{CAL} to the present calibrations has been estimated from the model described above. Fig. 10 shows the uncertainty $u(|k_{\mathrm{CAL}}|)$ as a function of $|V_{\mathrm{CAL}}|$ for three of the considered frequency.

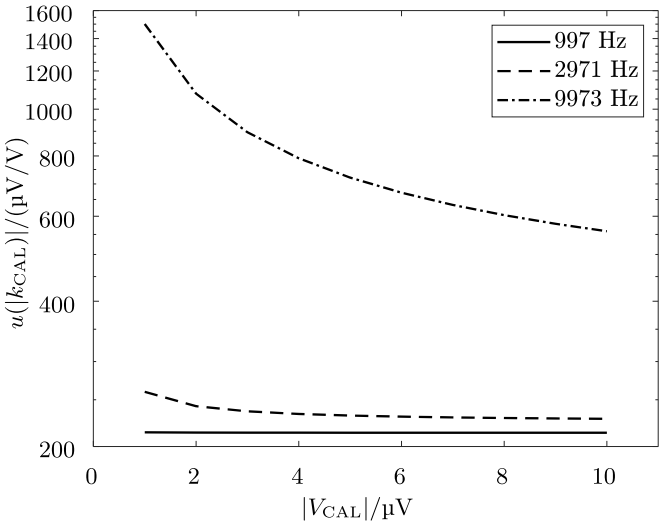

Fig. 10. Uncertainty of $u(|k_{\mathrm{CAL}}|)$ as a function of $|V_{\mathrm{CAL}}|$ for three of the considered f_{CAL}.

REFERENCES

[1] M. L. Meade, "Advances in lock-in amplifiers," *J. Phys. E, Sci. Instrum.*, vol. 15, no. 4, pp. 395–403, Apr. 1982.

[2] M. L. Meade, *Lock-in Amplifiers: Principles and Applications* (IEE Electrical Measurement). London, U.K.: Peter Peregrinus, 1983.

[3] P. A. Probst and B. Collet, "Low-frequency digital lock-in amplifier," *Rev. Sci. Instrum.*, vol. 56, no. 3, pp. 466–470, Mar. 1985.

[4] P.-A. Probst and A. Jaquier, "Multiple-channel digital lock-in amplifier with PPM resolution," *Rev. Sci. Instrum.*, vol. 65, no. 3, pp. 747–750, Mar. 1994.

[5] J. H. Scofield, "Frequency-domain description of a lock-in amplifier," *Amer. J. Phys.*, vol. 62, no. 2, pp. 129–133, Feb. 1994.

[6] R. D. Middlebrook, "Measurement of loop gain in feedback systems," *Int. J. Electron.*, vol. 38, no. 4, pp. 485–512, Apr. 1975.

[7] M. E. Briggs, R. W. Gammon, and J. N. Shaumeyer, "Measurement of the temperature coefficient of ratio transformers," *Rev. Sci. Instrum.*, vol. 64, no. 3, pp. 756–759, Mar. 1993.

[8] H. Yao, K. Ema, H. Fukada, K. Takahashi, and I. Hatta, "AC nanocalorimeter for measuring heat capacity of biological macromolecules in solution," *Rev. Sci. Instrum.*, vol. 74, no. 9, pp. 4164–4168, Sep. 2003.

[9] G. de Graaf and R. F. Wolffenbuttel, "Lock-in amplifier techniques for low-frequency modulated sensor applications," in *IEEE Int. Instrum. Meas. Technol. Conf. Proc.*, May 2012, pp. 1745–1749.

[10] G. Macias-Bobadilla, J. Rodríguez-Reséndiz, G. Mota-Valtierra, G. Soto-Zarazúa, M. Méndez-Loyola, and M. Garduño-Aparicio, "Dual-phase lock-in amplifier based on FPGA for low-frequencies experiments," *Sensors*, vol. 16, no. 3, p. 379, Mar. 2016.

[11] K. Kishore and S. A. Akbar, "Evolution of lock-in amplifier as portable sensor interface platform: A review," *IEEE Sensors J.*, vol. 20, no. 18, pp. 10345–10354, Sep. 2020.

[12] L. K. Rodenbach, "The quantum anomalous Hall effect: Uses in electrical metrology and understanding residual dissipation," Ph.D. dissertation, Dept. Phys., Stanford Univ., Stanford, CA, USA, 2023. [Online]. Available: https://www.proquest.com/dissertations-theses/quantum-anomalous-hall-effect-uses-electrical/docview/2901809310/se-2

[13] H. Park et al., "Observation of fractionally quantized anomalous Hall effect," *Nature*, vol. 622, no. 7981, pp. 74–79, Oct. 2023.

[14] D. K. Patel et al., "Zero external magnetic field quantum standard of resistance at the 10–9 level," 2024, *arXiv:2410.13365*.

[15] Z. Lu et al., "Fractional quantum anomalous Hall effect in multilayer graphene," *Nature*, vol. 626, no. 8000, pp. 759–764, Feb. 2024.

[16] D. R. Miyazaki, M. J. C. Bonfim, R. D. Gonçalves, R. da Silva Ferraz, R. S. da Fonseca, and E. P. Ribeiro, "Lock-in amplifier impedance meter using a low-cost microcontroller," in *Proc. 4th Int. Symp. Instrum. Syst., Circuits Transducers (INSCIT)*, Aug. 2019, pp. 1–5.

[17] J. Xu, G. Meynants, and P. Merken, "Low-power lock-in amplifier for complex impedance measurement," in *Proc. 3rd Int. Workshop Adv. Sensors Interfaces*, Jun. 2009, pp. 110–114.

[18] F. Raso, A. Hortelano, and M. M. Izquierdo, "A calibration method of the linearity of lock in amplifiers," in *Proc. Conf. Precis. Electromagn. Meas. (CPEM)*, Jul. 2016, pp. 1–2.

[19] D. Corminboeuf, "Calibration of the absolute linearity of lock-in amplifiers," *IEEE Trans. Instrum. Meas.*, vol. 68, no. 6, pp. 2060–2065, Jun. 2019.

[20] A. Cultrera, D. Corminboeuf, V. D'Elia, N. T. M. Tran, L. Callegaro, and M. Ortolano, "A new calibration setup for lock-in amplifiers in the low frequency range and its validation in a bilateral comparison," *Metrologia*, vol. 58, no. 2, Apr. 2021, Art. no. 025001.

[21] D. Georgakopoulos, I. F. Budovsky, and S. P. Benz, "Evaluation of a Josephson arbitrary waveform synthesizer at low voltages for the calibration of lock-in amplifiers," *IEEE Trans. Instrum. Meas.*, vol. 70, pp. 1–7, 2021.

[22] E. Theocharous, "Absolute linearity characterization of lock-in amplifiers," *Appl. Opt.*, vol. 47, no. 8, p. 1090, 2008.

[23] EURAMET Project n. 1466. (2019). *Calibration of Lock-in Amplifiers*. [Online]. Available: www.euramet.org

[24] *Model SR850 DSP Lock-in Amplifier User Manual*, 2nd ed., Stanford Res. Syst., Sunnyvale, CA, USA, Jan. 2009.

[25] A. Cultrera, J. Medved, M. Ortolano, P. Durandetto, A. Sosso, and L. Callegaro, "Calibration of magnitude error of lock-in amplifiers and noise response," in *Proc. Conf. Precis. Electromagn. Meas. (CPEM)*, Jul. 2024, pp. 1–2.

[26] *Evaluation of Measurement Data–Guide to the Expression of Uncertainty in Measurement*, BIPM, IEC, IFCC, ILAC, ISO, IUPAC, IUPAP, OIML, 2008.

[27] Zurich Instrum. AG. *MFLI User Manual*. Accessed: Feb. 28, 2025. [Online]. Available: https://docs.zhinst.com/mfli_user_manual

[28] CPIM. *Mutual Recognition Arrangement (CIPM MRA) Key Comparison DataBase*. Accessed: Feb. 28, 2025. [Online]. Available: https://www.bipm.org/kcdb/

[29] D. W. Allan, "Should the classical variance be used as a basic measure in standards metrology?" *IEEE Trans. Instrum. Meas.*, vol. IM-36, no. 2, pp. 646–654, Jun. 1987.

[30] N. F. Zhang, "Allan variance of time series models for measurement data," *Metrologia*, vol. 45, no. 5, pp. 549–561, Oct. 2008.

[31] D. B. Percival, "A wavelet perspective on the Allan variance," *IEEE Trans. Ultrason., Ferroelectr., Freq. Control*, vol. 63, no. 4, pp. 538–554, Apr. 2016.

[32] T. J. Witt and N. E. Fletcher, "Standard deviation of the mean and other time series properties of voltages measured with a digital lock-in amplifier," *Metrologia*, vol. 47, no. 5, pp. 616–630, Oct. 2010.

[33] D. B. Percival and A. T. Walden, *Wavelet Methods for Time Series Analysis*. Cambridge, U.K.: Cambridge Univ. Press, 2000.

[34] *Model SR830 DSP Lock-in Amplifier User Manual*, 2nd ed., Stanford Res. Syst., Sunnyvale, CA, USA, Jan. 2011.

[35] D. B. Percival and A. T. Walden, *Spectral Analysis for Univariate Time Series*. Cambridge, U.K.: Cambridge Univ. Press, 2020.

[36] D. B. Percival, "Characterization of frequency stability: Frequency-domain estimation of stability measures," *Proc. IEEE*, vol. 79, no. 7, pp. 961–972, Jul. 1991.

[37] F. W. J. Olver et al., "NIST digital library of mathematical functions," *Ann. Math. Artif. Intell.*, vol. 38, pp. 105–119, May 2003. [Online]. Available: https://dlmf.nist.gov/

[38] R. Lapuh, *Sampling with 3458A: Understanding, Programming, Sampling and Signal Processing*. New York, NY, USA: Left Right, 2018.

[39] P. Espel, A. Poletaeff, and A. Bounouh, "Characterization of analogue-to-digital converters of a commercial digital voltmeter in the 20 HZ to 400 HZ frequency range," *Metrologia*, vol. 46, no. 5, pp. 578–584, Sep. 2009, doi: 10.1088/0026-1394/46/5/023.

[40] R. L. Swerlein, "A 10 ppm accurate digital AC measurement algorithm," in *Proc. NCSL*, 1991, pp. 17–36.

[41] R. Lapuh and R. Lapuh, "Keysight 3458A frequency response model identification," in *Proc. Conf. Precis. Electromagn. Meas. (CPEM)*, Jul. 2018, pp. 1–2.

Alessandro Cultrera was born in 1981. He received the M.Sc. degree in physics and the Ph.D. degree in materials sciences from Università degli Studi di Torino, Turin, Italy, in 2010 and 2014, respectively.

He has been with the Istituto Nazionale di Ricerca Metrologica (INRIM), Turin, since 2014, working on the electrical characterization of nano-structured materials, precision electronic measurements, and novel calibration methods. He worked extensively on the development of electrical resistance tomography as a quantitative technique applied to thin-film and 2-D and nano-structured materials, and published about graphene, nanowire networks, and transparent conducting oxides. He is also active in the field of the calibration of instrumentation for signal recovery and impedance spectroscopy for metrology and energy storage (supercaps). He has been recently involved in measurements and traceability of electric power in nonsinusoidal distorted regimes.

Dr. Cultrera is a member of the European Metrology Network for Clean Energy and participates in the IEC/TC 113 "Nanotechnology for electrotechnical products and systems" for which he is the leader of two standardization projects on electrical characterization of graphene.

Juan Medved (Graduate Student Member, IEEE) was born in 1997. He received the master's degree in electronics engineering from the Universidad Tecnológica Nacional (UTN-FRBA), Buenos Aires, Argentina, in 2022. He is currently pursuing the Ph.D. degree in electrical, electronics, and communications engineering with the Politecnico di Torino, Turin, Italy, with a focus on quantum electrical impedance metrology.

He worked at the Quantum Metrology Group, Instituto Nacional de Tecnología Industrial (INTI), Buenos Aires, and since 2023, he has been working with the Quantum Electronics and Nano Technologies Department, Istituto Nazionale di Ricerca Metrologica (INRIM), Turin. His research interests include quantum Hall devices, Josephson standards, and impedance metrology.

Paolo Durandetto was born in 1986. He received the M.Sc. degree in physics of fundamental interactions from the University of Turin, Turin, Italy, in 2011, the master's thesis delved into the application of cosmic rays for detecting high atomic number materials hidden in a closed volume, and the Ph.D. degree in metrology from the Politecnico di Torino, Turin, in 2019.

In 2014, he joined the Istituto Nazionale di Ricerca Metrologica (INRIM), Turin, within the Quantum Electricity Sector. He was the Head of the Quantum Voltage Laboratory, he is also responsible for the Italian primary dc voltage standard based on the Josephson effect. He is also engaged in the development, application, and uncertainty assessment of high-accuracy measurement systems for general electrical quantities. His current research mostly revolves around the development and application of quantum voltage standards based on the Josephson effect for both dc and ac electrical metrology.

Massimo Ortolano was born in 1969. He received the M.Sc. degree in electronic engineering and the Ph.D. degree in metrology from the Politecnico di Torino, Turin, Italy, in 1997 and 2001, respectively.

Since 2000, he has been with the Department of Electronics and Telecommunications, Politecnico di Torino, where he is currently an Associate Professor. He teaches classes about electronic measurements and sensors. Since 2006, he has been collaborating with the Istituto Nazionale di Ricerca Metrologica (INRIM), Turin, with a focus on noise metrology, modeling of quantum Hall effect devices, and impedance metrology, and he has been visiting researcher at several national metrology institutes worldwide. His research interests also include low current measurements, fundamental constants, time and frequency metrology, and statistical methods for the evaluation of uncertainty.

Andrea Sosso is with the Istituto Nazionale di Ricerca Metrologica (INRIM), Turin, Italy, where he has developed quantum standards of resistance and dc/ac voltage, including the Italian Josephson standard, systems for dimensional small-scale metrology, fundamental constants determination, dedicated cryogenics, optical setups. He has led the participation in several international projects; is a referee for international journals; a member of Italian and international technical committees; has authored/co-authored more than a 100 peer-reviewed publications; tutored Ph.D. and graduation theses; and holds four patents.

Luca Callegaro (Member, IEEE) was born in 1967. He received the Ph.D. degree in physics from Politecnico di Milano, Milano, Italy, in 1996.

He was an Electronic Engineer. He has been with the Istituto Nazionale di Ricerca Metrologica (INRIM), Turin, Italy, since 1996, where he currently serves as the Head of the Quantum Electronics section. He has authored about 120 articles in international reviews and the book *Electrical Impedance: Principles, Measurement and Applications* 2012. He is responsible for the Italian National standards of electrical capacitance, inductance, ac resistance, and ac voltage ratio.

Dr. Callegaro is the Italian Deputy Delegate to EURAMET, the European Association of the National Metrology Institutes, and the contact person of its Technical Committee for Electricity and Magnetism (TC-EM), in which he served four years as Chairperson. He is the Italian Delegate to the Consultative Committee for Electricity and Magnetism (CCEM) of the International Committee for Weights and Measures (CIPM) and the Vice-Chair of the Technical Committee TC4—Measurement of Electrical Quantities—of the International Measurement Confederation (IMEKO).